Hyperpolarized [1-^{13}C]pyruvate-to-[1-^{13}C]lactate conversion is rate-limited by monocarboxylate transporter-1 in the plasma membrane

Yi Rao[a], Seth Gammon[a], Niki M. Zacharias[b], Tracy Liu[a], Travis Salzillo[a], Yuanxin Xi[c], Jing Wang[c], Pratip Bhattacharya[a], and David Piwnica-Worms[a,1]

[a]Department of Cancer System Imaging, University of Texas MD Anderson Cancer Center, Houston, TX 77030; [b]Department of Urology, University of Texas MD Anderson Cancer Center, Houston, TX 77030; and [c]Department of Biostatistics, University of Texas MD Anderson Cancer Center, Houston, TX 77030

Edited by Ralph J. DeBerardinis, University of Texas Southwestern Medical Center, Dallas, TX, and accepted by Editorial Board Member Rakesh K. Jain July 14, 2020 (received for review February 25, 2020)

Hyperpolarized [1-^{13}C]pyruvate magnetic resonance spectroscopic imaging (MRSI) is a noninvasive metabolic-imaging modality that probes carbon flux in tissues and infers the state of metabolic reprograming in tumors. Prevailing models attribute elevated hyperpolarized [1-^{13}C]pyruvate-to-[1-^{13}C]lactate conversion rates in aggressive tumors to enhanced glycolytic flux and lactate dehydrogenase A (LDHA) activity (Warburg effect). By contrast, we find by cross-sectional analysis using genetic and pharmacological tools in mechanistic studies applied to well-defined genetically engineered cell lines and tumors that initial hyperpolarized [1-^{13}C]pyruvate-to-[1-^{13}C]lactate conversion rates as well as global conversion were highly dependent on and critically rate-limited by the transmembrane influx of [1-^{13}C]pyruvate mediated predominately by monocarboxylate transporter-1 (MCT1). Specifically, in a cell-encapsulated alginate bead model, induced short hairpin (shRNA) knockdown or overexpression of MCT1 quantitatively inhibited or enhanced, respectively, unidirectional pyruvate influxes and [1-^{13}C]pyruvate-to-[1-^{13}C]lactate conversion rates, independent of glycolysis or LDHA activity. Similarly, in tumor models in vivo, hyperpolarized [1-^{13}C]pyruvate-to-[1-^{13}C]lactate conversion was highly dependent on and critically rate-limited by the induced transmembrane influx of [1-^{13}C]pyruvate mediated by MCT1. Thus, hyperpolarized [1-^{13}C]pyruvate MRSI measures primarily MCT1-mediated [1-^{13}C]pyruvate transmembrane influx in vivo, not glycolytic flux or LDHA activity, driving a reinterpretation of this maturing new technology during clinical translation. Indeed, Kaplan–Meier survival analysis for patients with pancreatic, renal, lung, and cervical cancers showed that high-level expression of MCT1 correlated with poor overall survival, and only in selected tumors, coincident with LDHA expression. Thus, hyperpolarized [1-^{13}C]pyruvate MRSI provides a noninvasive functional assessment primarily of MCT1 as a clinical biomarker in relevant patient populations.

hyperpolarized NMR | MCT1 | [1-^{13}C]pyruvate | monocarboxylate transporters | imaging biomarker

Reprogramming energy metabolism during cancer progression has emerged as a hallmark of cancer, initiating an extensive characterization of cancer metabolism (1). Conventional orthodoxy holds that cancers exhibit enhanced aerobic glycolysis, known as the Warburg effect (1), and enhanced glucose uptake and utilization have been identified as one of the cancer-associated metabolic signatures (2–6). The molecular basis of the Warburg effect has been linked to activation of the *myc* and *ras* oncogenes, upregulation of the PI3K/mTOR pathway, loss of PTEN expression, with a subsequent increase in aerobic glycolysis and lactate by lactate dehydrogenase A (LDHA) activity (7–9). These unique properties of enhanced glucose uptake and lactate production have created opportunities for cancer metabolic imaging (10). [^{18}F]Fluorodeoxyglucose positron emission tomography (FDG-PET) is the only Food and Drug Administration-approved metabolic-imaging modality that monitors local glucose uptake and phosphorylation (11). While [^{18}F]FDG-PET is widely used in oncologic metabolic imaging, it lacks specificity, with competing signals also arising from inflammatory foci and selected normal tissues with high glucose consumption (12). Furthermore, [^{18}F]FDG-PET fails to capture the downstream metabolic fates of substrates of the glycolytic pathway, which can be important for cancer characterization and prognosis (13). Hyperpolarized magnetic resonance spectroscopic imaging (MRSI) with ^{13}C-labeled substrates has gained traction as a noninvasive metabolic-imaging modality that can potentially map the reaction of specific metabolic substrates in vivo with a >10,000-fold increase in sensitivity compared with standard magnetic resonance spectroscopy (MRS) (14–22). Because pyruvate is at the crossroad of glucose fermentation and oxidative phosphorylation, the fate of [1-^{13}C]pyruvate could, in principle, be informative for the state of metabolic reprograming and carbon flux in a range of tumors. Indeed, full characterization of [1-^{13}C]pyruvate-to-[1-^{13}C]lactate conversion via LDHA (23) has been reported to correlate with cancer prognosis (5, 8).

The process of hyperpolarized [1-^{13}C]pyruvate MRSI requires a bolus injection of exogenous [1-^{13}C]pyruvate into the subject (animal or human). The injected pyruvate must first traverse vascular and extracellular spaces and then enter into intracellular spaces, wherein intracellular [1-^{13}C]pyruvate coupled with NADH are converted to [1-^{13}C]lactate and NAD$^+$ via cytoplasmic LDHA, resulting in a characteristic chemical shift in [1-^{13}C] detected by NMR (Fig. 1*A*). Since increased [1-^{13}C]pyruvate-to-[1-^{13}C]lactate

Significance

Hyperpolarized [1-^{13}C]pyruvate magnetic resonance spectroscopic imaging (MRSI), which measures [1-^{13}C]pyruvate-to-[1-^{13}C]lactate conversion, has been widely explored as a metabolic-imaging modality interpreted to reflect LDHA activity and glycolytic flux. However, we show definitively that hyperpolarized [1-^{13}C]pyruvate-to-[1-^{13}C]lactate conversion rates are primarily a functional readout of [1-^{13}C]pyruvate transmembrane influx mediated by MCT1, providing a mechanistic reinterpretation and redirection of clinical translation.

Author contributions: Y.R., S.G., N.M.Z., P.B., and D.P.-W. designed research; Y.R., N.M.Z., and T.S. performed research; Y.R., S.G., P.B., and D.P.-W. contributed new reagents/analytic tools; Y.R., S.G., N.M.Z., Y.X., J.W., P.B., and D.P.-W. analyzed data; and Y.R., S.G., T.L., P.B., and D.P.-W. wrote the paper.

The authors declare no competing interest.

This article is a PNAS Direct Submission. R.J.D. is a guest editor invited by the Editorial Board.

[1]To whom correspondence may be addressed. Email: dpiwnica-worms@mdanderson.org.

This article contains supporting information online at https://www.pnas.org/lookup/suppl/doi:10.1073/pnas.2003537117/-/DCSupplemental.

First published August 24, 2020.

conversion is considered to be a manifestation of enhanced aerobic glycolysis, many studies have proposed the application of hyperpolarized [1-^{13}C]pyruvate as a metabolic-imaging probe monitoring the Warburg effect downstream of glucose uptake and hexokinase activity (glucose phosphorylation) (24–27). Although most analyses attribute the observed elevation in hyperpolarized [1-^{13}C]pyruvate-to-[1-^{13}C]lactate conversion to increased LDHA activity and glycolytic flux (8, 28–31), the quantitative impact of transmembrane pyruvate influx has not been fully elucidated. Mediated primarily via monocarboxylate transporter (MCT) family members encoded by the SLC16 gene family (32), 14 MCT-related genes and their protein products have been identified in mammals. Seven MCTs have been functionally characterized, with particular attention focused on the transport physiology of MCT1, MCT2, and MCT4 (33). Although MCT1 ($K_{m,\ pyruvate}$, ~1 mM), MCT2 ($K_{m,\ pyruvate}$, ~0.1 mM), and MCT4 ($K_{m,\ pyruvate}$, ~153 mM)

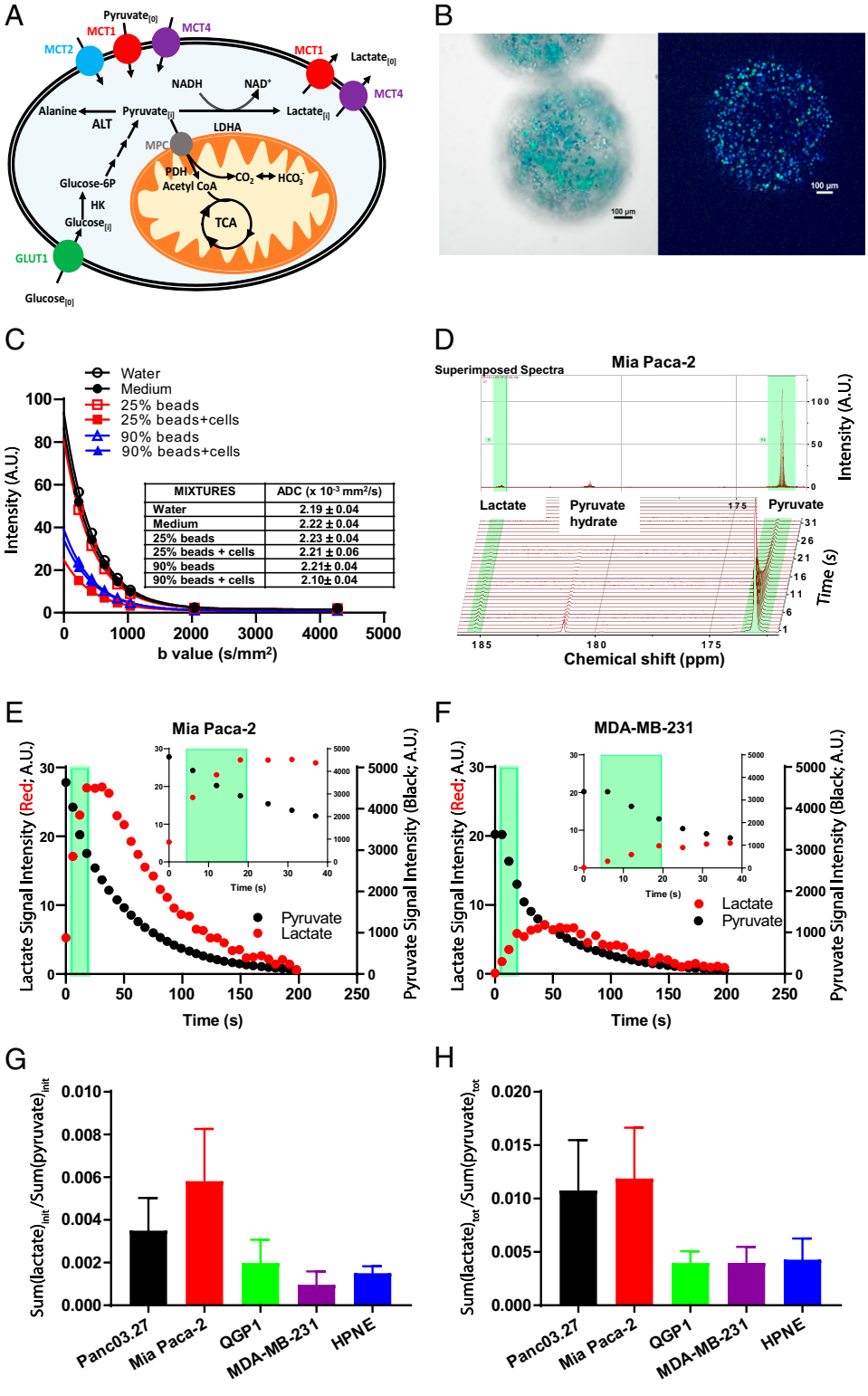

Fig. 1. Evaluating hyperpolarized [1-^{13}C]pyruvate-to-[1-^{13}C]lactate conversion rates in cellulo. (*A*) The model for [1-^{13}C]pyruvate-to-[1-^{13}C]lactate conversion via LDHA. Extracellular pyruvate (pyruvate$_{[0]}$) is transported into cells via MCTs. Pyruvate can be converted to lactate by LDHA. Intracellular lactate (Lactate$_{[i]}$) is exported out of cells via MCT1 and MCT4. (*B*) Microscopic images of green fluorescent protein (GFP) expressing Mia Paca-2 cell-encapsulated alginate beads. Cell nuclei were stained with Hoechst dye. (*Left* and *Right*) Epifluorescent image (*Left*) and midplane confocal image (*Right*). (Scale bar: 100 µm.) (*C*) DWI assessing ADCs of medium/bead mixtures. MRI signal intensity and calculated ADC (× 10^{-3} mm^2/s) of water, medium, beads (with/without cells) in medium at 25 and 90% by volume at various *b* values. (*D*) Using Mia Paca-2 cell-encapsulated alginate beads, NMR spectra of hyperpolarized [1-^{13}C]pyruvate and hyperpolarized [1-^{13}C]lactate interrogated over repetitive 6-s time intervals. (*E* and *F*) Signal intensities of hyperpolarized [1-^{13}C]pyruvate and hyperpolarized [1-^{13}C]lactate over time. The light green band demarcates the time intervals (6 to 18 s; *Inset*, expanded time scale) for the initial rate calculation of lactate production and pyruvate conversion. (*E*) Mia Paca-2 cells. (*F*) MDA-MB-231 cells. (*G*) Initial hyperpolarized [1-^{13}C]pyruvate-to-[1-^{13}C]lactate conversion rates in cellulo; the sum of converted hyperpolarized [1-^{13}C]lactate during the first 6 to 18 s normalized to the sum of hyperpolarized [1-^{13}C]pyruvate during the first 6 to 18 s across the cell panel. (*H*) Total hyperpolarized [1-^{13}C]pyruvate-to-[1-^{13}C]lactate conversion rates in cellulo; the sum of total converted hyperpolarized [1-^{13}C]lactate over 0 to 198 s normalized to the sum of hyperpolarized [1-^{13}C]pyruvate over 0 to 198 s across the cell panel. Error bars represent SD. A.U., arbitrary units.

are expressed in a tissue-distributed manner to mediate pyruvate influx, MCT1 is the most ubiquitously expressed among all cell types, while MCT2 is the most efficient pyruvate transporter (Fig. 1*A*) (32). Contradictory reports of whether hyperpolarized [1-^{13}C]pyruvate transmembrane transport is rate-limiting when evaluating the [1-^{13}C]pyruvate-to-[1-^{13}C]lactate conversion rate have been published (34, 35). While these various correlation studies are noteworthy, there remains a need for a rigorous mechanism-based examination of whether MCT1 is rate-limiting for hyperpolarized [1-^{13}C]pyruvate influx or not.

The existence of membrane-limited transport is a fundamental open question in the field that underpins interpretation of all preclinical studies, and importantly, as the technology begins to migrate to the clinic, also patient studies (18, 36–39). This unfilled need led us to rigorously evaluate the contribution of transmembrane barrier function to pyruvate influx and what the conversion to lactate implied, with a deliberate focus on human cancer cells. We hypothesized that pyruvate influx mediated by MCTs provides the first upstream cellular barrier to the conversion of [1-^{13}C]pyruvate to [1-^{13}C]lactate, and therefore, using hyperpolarized [1-^{13}C]pyruvate-to-[1-^{13}C]lactate conversion rates without taking into account the expression and transport function of MCTs renders an incomplete assessment of the metabolic signatures of tumors. Herein, using genetic and pharmacologic tools in mechanistic studies on well-defined cell lines and tumors, we demonstrated that initial hyperpolarized [1-^{13}C]pyruvate-to-[1-^{13}C]lactate conversion rates were highly dependent on and rate-limited by the transmembrane influx of pyruvate, dominated by MCT1.

Methods

All methods are detailed in *SI Appendix, Methods*.

Cell Culture and Cell Lines. Mia Paca-2, Panc03.27, MDA-MB-231, and hTERT-HPNE cells were obtained from the American Type Culture Collection. QGP1 cells were purchased from the Japanese Collection of Research Bioresources cell bank. All cells were maintained based on recommended culturing conditions (*SI Appendix, Methods*).

Stable Knockdown and Overexpression of MCT1. For stable MCT1 knockdown, Mia Paca-2 and Panc03.27 cells were transduced with SMARTvector inducible human SLC16A1 hEF1a-TurboGFP short hairpin RNA (shRNA) lentiviral targeting MCT1 or SMARTvector Inducible Non-Targeting Control hEF1α/TurboGFP per manufacturer recommended protocol (Dharmacon) (*SI Appendix, Methods*). For stable overexpression of MCT1 in QGP1 and Mia Paca-2 MCT1 knockdown sequence (KD_i) cells, Precision LentiORF Human SLC16A1 GFP lentiviral particles or Precision LentiORF RFP Positive Control particles (Dharmacon) were used for transduction.

Messenger RNA Sequencing. Messenger RNA (mRNA) was extracted and purified from each cell line using the RNeasy Kit per manufacturer instructions (Qiagen). mRNA samples were sequenced using the Illumina HighSeq Sequencing platform at MD Anderson Next Generation Sequencing Core.

Western Blotting. Lysed cells were either directly used as whole-cell lysate or underwent membrane fractionation to separate membrane and cytoplasmic subcellular fractions using a commercial Cell Fractionation Kit (Cell Signaling Technology). Equal aliquots of lysate were loaded into protein resolving gels followed by membrane transfer. Posttransferred nitrocellulose membranes were stained in Ponceau S staining solution to evaluate total protein loading (*SI Appendix*, Fig. S1). Membranes were probed with primary antibodies at 4 °C overnight: MCT1 (Thermo Fisher Scientific), MCT2 (Novus Biologicals), MCT4 (Boster), LDHA (R&D System), Na/K-ATPase (Abcam), and GAPDH (Abcam). Thereafter, secondary anti-mouse or anti-rabbit horseradish peroxidase-conjugated Immunoglobulin G antibodies (BioRad) were incubated for 1 h at room temperature, and protein bands were developed with chemiluminescent reagents (*SI Appendix, Methods*).

Real-Time Quantitative PCR Assays. RNA was extracted from cells with the Direct-zol RNA Kit (Zymo Research). Complementary DNA (cDNA) was synthesized using Maxima First Strand cDNA Synthesis Kit for RT-qPCR (Thermo Fisher Scientific). Real-time quantitative PCR was performed with primers for MCT1 and GAPDH (Sigma-Aldrich) (*SI Appendix, Methods*). DNA amplification was quantified with SYBR green (BioRad) on a CFX96 Touch Real-Time PCR Detection System (BioRad).

In Vitro Analysis of Extracellular Acidification Rate. The Seahorse XF glycolysis stress assay was used to measure baseline extracellular acidification rates (ECARs). Cell lines were seeded on XF96 Cell Culture Microplates (Seahorse Bioscience) 48 h before each experiment. During the Seahorse experiment, cells were maintained in Dulbecco's modified Eagle's medium (DMEM) lacking $NaHCO_3$, supplemented with 2 mM glutamine, 5 mM glucose, and adjusted to pH 7.4. Data were normalized to cellular DNA as stained with Hoechst 33342 (Thermo Fisher Scientific) and imaged by an Operetta High-Content Imaging System (PerkinElmer). Measured baseline ECAR data in the cell panel were normalized to Panc03.27 values (*SI Appendix, Methods*).

Pyruvate or Lactate Content and Pyruvate Influx Assay. Cells were seeded into 96-well black wall clear bottom plates. Doxycycline-inducible cell lines were supplemented with doxycycline for 48 h. On the day of the experiment, cells were incubated in DMEM containing 0 or 10 mM sodium pyruvate for 6 s at 37 °C, followed by ice-cold phosphate-buffered saline washes. A fluorimetric assay using a Pyruvate Assay Kit or Lactate Assay Kit (Sigma-Aldrich) was used to assess cellular pyruvate or lactate content at $\lambda_{excitation}$ = 535/$\lambda_{emission}$ = 587 nm, wherein the difference in cellular pyruvate between 0 or 10 mM exogenous sodium pyruvate represented pyruvate influx. Calculated pyruvate content and influx data were normalized to cellular DNA as stained with Hoechst 33342 (Thermo Fisher Scientific) (*SI Appendix, Methods*).

LDHA Activity Assay. For determination of LDHA activity in a 96-well plate format, 25 μL of cell-extracted LDHA, 125 μL of tris(hydroxymethyl)aminomethane (Tris)/NaCl/NADH buffer, and 25 μL of Tris/NaCl/pyruvate solution with various pyruvate concentrations added per well was performed as per instructions for a LDHA Assay Kit (Sigma-Aldrich). Absorbance of NADH at 340 nm was measured five times with 30-s intervals (*SI Appendix, Methods*).

NAD^+/NADH Assay. Cells with or without doxycycline treatment were seeded at a density of 5.0×10^4 cells/well into 96-well black wall clear bottom plates and allowed to attach overnight. The NAD/NADH-Glo Assay was used to assess NAD^+ and NADH levels per kit instructions (Promega) (*SI Appendix, Methods*).

Cell Encapsulation. Alginate solution (2.7% wt/vol) was mixed with 2.5×10^7 cells and transferred into a 1-mL syringe clamped to a pump (Harvard Apparatus) (*SI Appendix, Methods* and Fig. S2). A 5-kV voltage was applied between the alginate mixture and a flask containing $CaCl_2$/NaCl solution. Cell-encapsulated alginate beads were formed upon passage through the electromagnetic field and stabilized by cross-linking induced by the $CaCl_2$ solution (*SI Appendix, Methods*).

Diffusion-Weighted MRI. [^{1}H] MRI was performed using a 7 T Bruker Biospec MR system with BGA-12 gradient systems in a ^{1}H volume coil with 35-mm inner diameter (Bruker). A conical tube filled with either water or hyperpolarization medium alone, 25 or 90% alginate beads with or without cells by volume, was mixed and placed in the center of the ^{1}H volume coil. A standard diffusion measurement was executed on all phantoms at b = 233, 435, 636, 837, 1,037, 2,040, and 4,272 s/mm^2, and curve-fit of the T2 signal versus b values was used to determine bulk apparent diffusion coefficient (ADC) values (*SI Appendix, Methods*).

In Vitro Hyperpolarization Experiments Using Vertical Bore NMR. Cell-encapsulated alginate beads (1 mL) were resuspended in 2.5 mL of assay medium in a 10 mm screw-cap NMR tube (Wilmad-LabGlass). Experiments were conducted in a 7 T Bruker BioSpin NMR spectrometer (Billerica) with a 10-mm broadband probe running TopSpin 3.5 software. An aliquot of 26.5 mg of a pyruvic acid mix was polarized in a HyperSense DNP system (Oxford Instruments) as described in published procedures (40). The frozen hyperpolarized [1-^{13}C]pyruvic acid was then dissolved in 4 mL of the dissolution medium at 180 °C (40). At time 0 of acquisition, 500 μL of the hyperpolarized [1-^{13}C]pyruvic acid stock (37 mM) was injected into the cell-encapsulated alginate bead solution in the NMR tube resulting in a fnal concentration of ∼4.7 mM. Single consecutive ^{13}C scans were acquired (*SI Appendix, Methods*). Samples of cell-encapsulated alginate bead solution were then subjected to Alamar Blue Assay (Thermo Fisher Scientific) to confirm cell viability except for the digitonin-treated permeabilized samples. Initial hyperpolarized [1-^{13}C]pyruvate-to-[1-^{13}C]lactate

conversion rate $= \frac{Sum([1-^{13}C]lactate)(6-18s)}{Sum([1-^{13}C]pyruvate)(6-18s)}$. Total hyperpolarized [1-^{13}C]pyruvate-to-[1-^{13}C]lactate conversion $= \frac{Sum([1-^{13}C]lactate)(0-198s)}{Sum([1-^{13}C]pyruvate)(0-198s)}$.

Xenografts Tumor Models. Animal experiments were performed in compliance with protocols approved by the Institutional Animal Care and Use Committee of MD Anderson Cancer Center. A mixture of DMEM and Matrigel (BD Bioscience) (1:1 ratio) containing 2×10^6 Mia Paca-2 doxycycline-inducible MCT1 knockdown cells or Mia Paca-2 doxycycline-inducible nontargeting control (NTC) cells were injected subcutaneously into the right hind legs of 8- to 12-wk-old female athymic C57BL/6-nu/nu mice (Charles River Laboratories). When tumor volumes reached ∼250 mm^3, mice from paired groups were subjected to predoxycycline MRI/hyperpolarized [1-^{13}C]pyruvic acid MRS. Immediately after the imaging session, paired groups of mice were supplemented with freshly dissolved doxycycline (1 mg/mL in 5% sucrose water) for ∼7 to 14 d to induce MCT1 knockdown or NTC expression. Postdoxycycline, MRI/hyperpolarized [1-^{13}C]pyruvic acid MRS experiments were performed on the same animal. Upon completion of imaging, mice were killed, and tumors were harvested for immunohistochemical analysis.

In Vivo Hyperpolarization Experiments Using MRSI. [^{1}H] MRI was performed using a 7 T Bruker Biospec small animal MR system with BGA-12 gradients in a ^{1}H volume coil with 72-mm inner diameter (Bruker). Concurrently, hyperpolarized [1-^{13}C]pyruvic acid magnetic resonance spectra were measured using a ^{13}C Doty Scientific (Doty Scientific) transmit/receive surface coil placed over the established tumor. Before imaging, animals were anesthetized and placed on a water-heated imaging sled. An 8 M ^{13}C-urea capillary phantom was placed above the surface coil for chemical-shift referencing (41). Animal positioning was confirmed, and the tumor location was identified (*SI Appendix, Methods*). For ^{13}C spectroscopy measurements, the ^{13}C channel was tuned and set to acquire ^{13}C signal every 2 s for 3 min (*SI Appendix, Methods*). Similar to in vitro hyperpolarization experiments, the [1-^{13}C]pyruvate acid was hyperpolarized and dissolved. MRS acquisition was initiated ∼15 s prior to injection of 200 μL of ∼60 mM standard hyperpolarized [1- ^{13}C]pyruvic acid solution via tail vein bolus injection. The majority of [1-^{13}C]pyruvic acid mixtures were polarized using a HyperSense DNP system (Oxford Instruments), the same as described in *In Vitro Hyperpolarization Experiments Using Vertical Bore NMR*, while a few hyperpolarized [1- ^{13}C]pyruvic acid mixtures were polarized in a SPINlab system (General Electric). Above baseline hyperpolarized [1-^{13}C]pyruvate-to-[1-^{13}C]lactate conversion $= \frac{Sum([1-^{13}C]lactate)(above\ baseline)}{Sum([1-^{13}C]pyruvate)(above\ baseline)}$.

Survival Analysis. Datasets from the Human Protein Atlas (HPA) were used to compare mRNA expression of MCTs between normal and cancer tissues and to determine the overall survival of patients with pancreatic, renal, lung, and cervical cancers. Gehan–Breslow–Wilcoxon and log-rank tests were used to estimate *P* values between high- and low-expression groups. χ^2 tests were used to test the association between MCT1 and LDHA expression profiles with high-, medium-, and low-expression levels for each cancer.

Statistical Analysis. For normalization analysis, cellular data were normalized to Panc03.27 values across the cell panel. The Pearson test was used to assess correlations, and the likelihood ratio test *P* values were reported. A paired *t* test was used to evaluate the difference between paired initial [1-^{13}C]pyruvate-to-[1-^{13}C]lactate conversion rates both in cellulo and in vivo, and the likelihood ratio test *P* values were reported.

Results

Pyruvate Influx and the Role of MCTs in [1-^{13}C]Pyruvate-to-[1-^{13}C] Lactate Conversion Rates. We sought to rigorously examine the relationships between the initial conversion rates of hyperpolarized [1-^{13}C]pyruvate-to-[1-^{13}C]lactate, glycolysis, LDHA, and pyruvate influx to test the hypothesis that the apparent conversion of [1-^{13}C]pyruvate-to-[1-^{13}C]lactate catalyzed by LDHA would be restricted by cell surface-mediated [1-^{13}C]pyruvate influx. We used a cross-sectional experimental study design with a multicell-line panel that consisted of four well-established cancer cell lines and one normal cell line, which included a K-RAS mutant human pancreatic cancer cell line (Mia Paca-2; K-RASG12C), a K-RAS wild-type pancreatic cancer cell line (Panc03.27; wt K-RAS), a human pancreatic neuroendocrine cancer cell line (QGP1), a human triple negative breast cancer cell line (MDA-MB-231), as well as a human immortalized normal pancreatic epithelial cell line (HPNE).

Cells in suspension receive different extracellular-matrix signals, often impacting metabolic profiles compared with adherent cells (42). Thus, we exploited cell-encapsulated alginate beads (Fig. 1*B*), which provided sufficient cell mass to enable rapid real-time MRS while maintaining a proper microenvironment for adherent cell metabolism. To confirm that the alginate matrix itself did not impose an extracellular diffusion barrier (43), diffusion-weighted imaging (DWI) was performed to estimate the ADC of water, hyperpolarization medium alone, medium containing various concentrations of alginate beads, and cell-encapsulated alginate beads from 25 to 90% per volume. The calculated bulk ADC values (Fig. 1*C*) for water, medium alone, medium with 25 or 90% beads, and medium with 25 or 90% cell-encapsulated beads per volume were not significantly different from each other ($P = 0.31$). Thus, we concluded that the ADC of the alginate matrix was indistinguishable from bulk water and did not impose significant diffusion limitations for delivery of [1-^{13}C]pyruvate into the extracellular spaces surrounding the embedded cells.

Next, to determine the initial rate of hyperpolarized [1-^{13}C]pyruvate-to-[1-^{13}C]lactate conversion in these isolated live cells, we measured the spectra of hyperpolarized [1-^{13}C]pyruvate and [1-^{13}C]lactate over time (Fig. 1*D*), and the initial area under the curves of hyperpolarized [1-^{13}C]lactate normalized to [1-^{13}C]pyruvate were integrated over the first 6 to 18 s. As examples, Mia Paca-2 cells exhibited enhanced hyperpolarized [1-^{13}C]lactate production (Fig. 1*E*) compared with MDA-MB-231 cells over the first 6 to 18 s (Fig. 1*F*). A [1-^{13}C]lactate-to-[1-^{13}C]pyruvate ratio over the first 6 to 18 s (spanning the near linear range) was calculated to estimate the initial normalized hyperpolarized [1-^{13}C]pyruvate-to-[1-^{13}C] lactate conversion rate (Fig. 1 *E* and *F*). Among the cell lines, Mia Paca2 cells had the highest conversion rate, ∼2-fold enhanced compared with Panc03.27, and >3-fold increased compared with QGP1, MDA-MB-231, or HPNE cells (Fig. 1*G*). We also calculated the total observed [1-^{13}C]lactate to total observed [1-^{13}C]pyruvate ratio over the entire time course of data collection (0- to 198-s time interval) to estimate total hyperpolarized [1-^{13}C]pyruvate-to-[1-^{13}C]lactate conversion; the general trend of total hyperpolarized [1-^{13}C]pyruvate-to-[1-^{13}C]lactate conversion across the cell panel was similar to that of the initial hyperpolarized [1-^{13}C]pyruvate-to-[1-^{13}C]lactate conversion rates (Fig. 1*H*). Hence, a [1-^{13}C]lactate-to-[1-^{13}C]pyruvate ratio over the first 6 to 18 s was used to estimate a normalized initial hyperpolarized [1-^{13}C]pyruvate-to-[1-^{13}C]lactate conversion rate throughout all hyperpolarized [1-^{13}C]pyruvate MRS experiments unless stated otherwise.

Hyperpolarized [1-^{13}C]pyruvate-to-[1-^{13}C]lactate conversion has been conventionally considered to correlate with cellular glycolysis (24–27). To independently measure glycolytic flux, the ECAR was used to semiquantitatively evaluate cellular glycolysis across the panel of cells. Baseline ECAR was highest in Pan03.27, Mia Paca-2, and MDA-MB-231 cells, followed by QGP1 cells, and lowest in nontransformed HPNE cells (Fig. 2*A*). We found no significant correlation between initial hyperpolarized [1-^{13}C]pyruvate-to-[1-^{13}C]lactate conversion rates and baseline ECAR across the cell panel ($r = -0.02$, $P = 0.97$; Fig. 2*B*). LDHA activity has also been correlated with hyperpolarized [1-^{13}C]pyruvate-to-[1-^{13}C]lactate conversion in many single-model preclinical studies (28–30). Herein, to evaluate rigorously the contribution of LDHA to hyperpolarized [1-^{13}C]pyruvate-to-[1-^{13}C]lactate conversion rates again across a broad cell panel, we first determined LDHA protein content in these cells by Western blot. MDA-MB-231 cells had the highest LDHA protein content followed by HPNE cells, whereas Panc03.27,

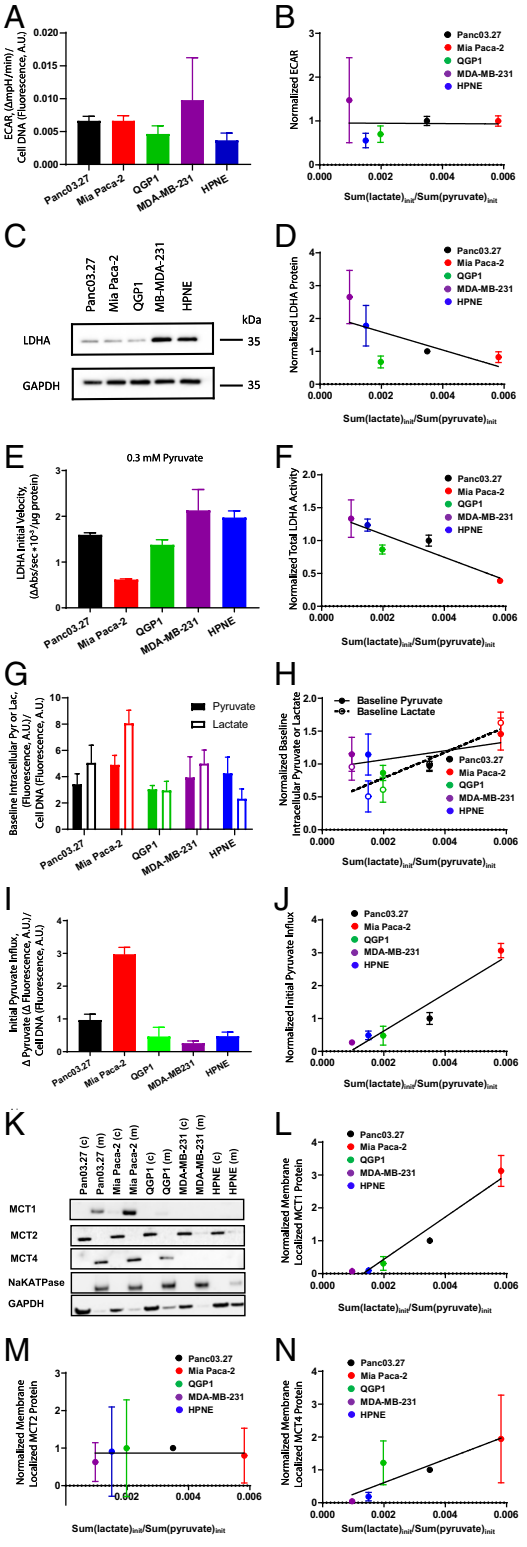

Fig. 2. Correlations between hyperpolarized [1-^{13}C]pyruvate-to-[1-^{13}C]lactate initial conversion rates and normalized ECAR, LDHA protein content, LDHA total activities, intracellular pyruvate and lactate, initial pyruvate unidirectional influxes, or MCT protein content across a panel of cell lines. Cellular data were normalized to Panc03.27 values across the cell panel. (*A*) Cellular glycolysis estimated by ECAR measurements across the cell panel. (*B*) Pearson correlation analysis between hyperpolarized [1-^{13}C]pyruvate-to-[1-^{13}C]lactate initial conversion rate and ECARs; $r_{(ECAR)} = -0.02$; $P = 0.97$. (*C*) Western blot showing LDHA protein content. (*D*) Pearson correlation analysis between hyperpolarized [1-^{13}C]pyruvate-to-[1-^{13}C]lactate initial conversion rate and LDHA protein contents; $r_{(LDHA\ protein)} = -0.65$; $P = 0.23$. (*E*) LDHA total enzymatic activities measured at 0.3 mM pyruvate. (*F*) Pearson correlation analysis between hyperpolarized [1-^{13}C]pyruvate-to-[1-^{13}C]lactate initial conversion rate and LDHA total enzymatic activities; $r_{(LDHA\ total\ activity)} = -0.91$; $P = 0.03$. (*G*) Intracellular pyruvate and lactate contents. Baseline pyruvate values are multiplied by a scaling factor of 10, and baseline lactate values are multiplied by a scaling factor of 0.1 for data presentation purposes. (*H*) Pearson correlation analysis between hyperpolarized [1-^{13}C]pyruvate-to-[1-^{13}C]lactate initial conversion rate and intracellular pyruvate content [$r_{(intracellular\ pyruvate)} = 0.59$; $P = 0.29$] or intracellular lactate content [$r_{(intracellular\ lactate)} = 0.85$; $P = 0.07$]. (*I*) Initial rates of pyruvate influx (6 s) in a panel of cells. (*J*) Pearson correlation analysis between hyperpolarized [1-^{13}C]pyruvate-to-[1-^{13}C]lactate initial conversion rate in cellulo and initial pyruvate influx; $r_{(pyruvate\ influx)} = 0.96$; $P = 0.01$. (*K*) Western blot showing membrane and cytosolic fractionations of MCT1, MCT2, and MCT4 protein across the cell line panel. (*L–N*) Pearson correlation analysis between hyperpolarized [1-^{13}C]pyruvate-to-[1-^{13}C]lactate initial conversion rate and membrane-bound MCT1 (*L*), MCT2 (*M*), or MCT4 protein (*N*); $r_{(MCT1)} = 0.98$, $P = 0.005$; $r_{(MCT2)} = 0.14$, $P = 0.83$; $r_{(MCT4)} = 0.89$, $P = 0.04$. A.U., arbitrary units.

Mia Paca-2, and QGP1 cells had low LDHA protein content (Fig. 2*C*). Importantly, we found no significant correlation between hyperpolarized [1-^{13}C]pyruvate-to-[1-^{13}C]lactate conversion rates and LDHA protein content across the cell panel ($r = -0.65$, $P = 0.23$; Fig. 2*D*). We also evaluated LDHA total enzymatic activity across the cell panel using enzyme extracts from these cells (Fig. 2*E*) and found that initial hyperpolarized [1-^{13}C]pyruvate-to-[1-^{13}C]lactate conversion rates negatively correlated with LDHA total enzymatic activity ($r = -0.91$, $P = 0.03$; Fig. 2*F*). Because the conversion of hyperpolarized [1-^{13}C]pyruvate-to-[1-^{13}C]lactate is a dynamic process, we sought to evaluate the effect of intracellular pyruvate or lactate pool size on hyperpolarized [1-^{13}C]pyruvate-to-[1-^{13}C]lactate conversion rates. The cell content of intracellular pyruvate and lactate were estimated using biochemical coupled-fluorimetric assays (Fig. 2*G*). We found no significant correlation between hyperpolarized [1-^{13}C]pyruvate-to-[1-^{13}C]lactate conversion rates and intracellular pyruvate content across the cell panel ($r = 0.59$, $P = 0.29$; Fig. 2*H*) or intracellular lactate content across the cell panel ($r = 0.85$, $P = 0.07$; Fig. 2*H*).

To independently estimate the initial unidirectional influx of pyruvate in the context of a hyperpolarized [1-^{13}C]pyruvate experiment, we performed zero-trans experiments. Briefly, during the initiation of a hyperpolarized [1-^{13}C]pyruvate experiment in vivo wherein a bolus infusion of hyperpolarized [1-^{13}C]pyruvate passes throughout the tissues and over the cells (44, 45), extracellular exogenous pyruvate concentration (>10 mM) is considerably larger than that of intracellular pyruvate (~0.2 to 0.45 μM). To simulate this condition, cells were exposed to media without or with exogenous pyruvate (10 mM) for 6 s, and the change in intracellular pyruvate was measured using a biochemical coupled-fluorimetric assay to estimate unidirectional pyruvate influx. Mia Paca-2 cells had the highest initial pyruvate influx, which was ~threefold higher than the second highest cell line, Panc03.27 cells, and ~six to ninefold higher than QGP1, MDA-MB-231, and HPNE cells (Fig. 2*I*). Initial pyruvate influx showed a strong correlation with the initial hyperpolarized [1-^{13}C]pyruvate-to-[1-^{13}C]lactate conversion rate ($r = 0.96$, $P = 0.01$; Fig. 2*J*). Taken together, these results suggested that hyperpolarized [1-^{13}C]pyruvate-to-[1-^{13}C]lactate conversion rates positively correlated with pyruvate influx but negatively correlated with LDHA total enzymatic activity across all tested cell lines.

Because the influx of pyruvate is primarily mediated by MCT1, -2, and -4, the contribution of each transporter protein to hyperpolarized [1-^{13}C]pyruvate-to-[1-^{13}C]lactate conversion rates was further examined. Because only plasma membrane-bound transporters are involved in pyruvate influx (46), we performed protein fractionation to determine if membrane-bound MCTs

correlated with [1-^{13}C]pyruvate-to-[1-^{13}C]lactate conversion rates. Western blot analysis showed that membrane-localized MCT1 content, which colocalized with the plasma membrane marker, Na/K-ATPase, was the highest in Mia Paca-2 cells, relatively lower in Panc03.27 cells, minimally detectable in QGP1 cells, and nondetectable in MDA-MB-231 as well as HPNE cells (Fig. 2*K*), directly correlating with the rank order of initial [1-^{13}C]pyruvate-to-[1-^{13}C]lactate conversion rates for the cell line panel ($r = 0.98$, $P = 0.005$; Fig. 2*L*). Protein contents of MCT2 were primarily localized in cytosolic fractionations across the cell panel, with membrane-bound MCT2 minimally detectable (Fig. 2*K*). There was no significant correlation between [1-^{13}C]pyruvate-to-[1-^{13}C]lactate conversion rates and membrane-localized MCT2 ($r = 0.14$, $P = 0.83$; Fig. 2*M*). The localization pattern of membrane-bound MCT4 was similar to that of MCT1 (Fig. 2*K*), and thus, membrane-bound MCT4 protein also correlated with hyperpolarized [1-^{13}C]pyruvate-to-[1-^{13}C]lactate conversion rate ($r = 0.89$, $P = 0.04$; Fig. 2*N*). The MCTs protein content of whole-cell lysates across the cell panel were also evaluated by Western blot. The overall total protein pattern was consistent with the sum of both cytosolic and membrane fractionations for MCT1 and MCT4 but less so for MCT2, implying a large perinuclear fraction for MCT2 (*SI Appendix*, Fig. S3*A*). Furthermore, when evaluating mRNA levels of MCTs, MCT1 mRNA expression demonstrated a similar expression pattern, matching the corresponding Western blot analysis. In contrast, MCT2 mRNA expression was low across all tested cell lines, while MCT4 mRNA expression was the highest in MDA-MB-231 cells followed by HPNE and Panc03.27, was detectable in Mia Paca-2 cells, but not detectable in QGP1 cells (*SI Appendix*, Fig. S3*B*), neither of which significantly correlated with their corresponding protein-content patterns. Overall, only MCT1 mRNA expression correlated with the measured hyperpolarized [1-^{13}C]pyruvate-to-[1-^{13}C]lactate conversion rate in cellulo ($r = 0.98$, $P = 0.004$; *SI Appendix*, Fig. S3*C*).

Overall analyses demonstrated that hyperpolarized [1-^{13}C]pyruvate-to-[1-^{13}C]lactate conversion rates were highly positively correlated with pyruvate influx, primarily mediated by MCTs. Considering the relatively high pyruvate affinity and abundance of MCT1 localized to the plasma membrane compared with MCT2 or MCT4, MCT1 was likely the primary transmembrane mediator of [1-^{13}C]pyruvate influx enabling access to cytosolic LDHA. Thus, we sought to further determine the impact of MCT1 on hyperpolarized [1-^{13}C]pyruvate-to-[1-^{13}C]lactate conversion rates.

Observed Hyperpolarized [1-^{13}C]Pyruvate-to-[1-^{13}C]Lactate Conversion Rates by MRS Are Dependent on and Rate-Limited by MCT1 in Live Cells. Because hyperpolarized [1-^{13}C]pyruvate-to-[1-^{13}C]lactate conversion rates were strongly correlated with pyruvate influx, the dependence of conversion rates on the major pyruvate transporter, MCT1, was further evaluated in live cell-encapsulated alginate beads enabling real-time MRS. In Mia Paca2 cell-encapsulated alginate beads, when MCT1 was pharmacologically inhibited by AZD3965, a potent and selective MCT1 and MCT2 inhibitor, hyperpolarized [1-^{13}C]lactate production was decreased (*SI Appendix*, Fig. S4 *A* and *B*). Initial rates of hyperpolarized [1-^{13}C]pyruvate-to-[1-^{13}C]lactate conversion were calculated showing that treatment with AZD3965 led to an ∼90% decrease in lactate production (Fig. 3*A*). Genetic knockdown of MCT1 was also used to interrogate the dependence of hyperpolarized [1-^{13}C]pyruvate-to-[1-^{13}C]lactate conversion rate on MCT1 expression. Two MCT1-expressing cell lines, Mia Paca-2 and Panc03.27, were stably transfected with a doxycycline-inducible lentiviral shRNA with either a MCT1 knockdown sequence (KD_i) or an NTC sequence (NTC_i) (*SI Appendix*, Fig. S5*A*). Incubating MCT1 KD_i cells with 500 ng/mL doxycycline for 48 h induced near-complete MCT1 knockdown in Mia Paca-2 and Panc03.27 cells at both transcriptional and membrane-localized protein levels (*SI Appendix*, Fig. S5 *C–F*). In contrast, cell lines containing the NTC_i sequence demonstrated no significant change in MCT1 protein levels regardless of doxycycline induction (*SI Appendix*, Fig. S5 *C–F*). Upon doxycycline induction, the initial [1-^{13}C]pyruvate-to-[1-^{13}C]lactate conversion rates significantly decreased ∼78% in Mia Paca-2 MCT1 KD_i cells (Fig. 3*B*), while there was no significant difference in [1-^{13}C]pyruvate-to-[1-^{13}C]lactate conversion in Mia Paca-2 NTC_i control cells (Fig. 3*B*). Similarly, [1-^{13}C]pyruvate-to-[1-^{13}C]lactate conversion rates significantly decreased ∼87% in Panc03.27 MCT1 KD_i cells upon doxycycline induction compared with the doxycycline-free control (Fig. 3*C*). By contrast, there was no statistically significant difference observed in Panc03.27 NTC_i control cells upon doxycycline induction (Fig. 3*C*). Overall, results from both pharmacological inhibition and genetic knockdown of MCT1 indicated that hyperpolarized [1-^{13}C]pyruvate-to-[1-^{13}C]lactate conversion rates critically depended on transmembrane transport of pyruvate mediated by MCT1 in live cells.

MDA-MB-231 cells had low hyperpolarized [1-^{13}C]pyruvate-to-[1-^{13}C]lactate conversion rates and low MCT1 expression but high LDHA protein levels (Figs. 1*G* and 2 *C* and *K*). To further examine whether the influx of hyperpolarized [1-^{13}C]pyruvate was rate-limiting for the production of [1-^{13}C]lactate, MDA-MB-231 cells were permeabilized with digitonin to enable pyruvate penetration regardless of MCT expression. A >7-fold increase in [1-^{13}C]pyruvate-to-[1-^{13}C]lactate conversion rates in digitonin-treated MDA-MB-231 cells was measured when compared with control cells (Fig. 3*D*). This further demonstrated that the measured [1-^{13}C]pyruvate-to-[1-^{13}C]lactate conversion rates were rate-limited by the influx of [1-^{13}C]pyruvate at the level of the plasma membrane.

To determine whether MCT1-mediated pyruvate transport was the rate-limiting step in the hyperpolarized [1-^{13}C]pyruvate-to-[1-^{13}C]lactate conversion process, we further modified the MCT1-knockdown Mia Paca-2 stable cell line (MCT1 KD_i). Herein, doxycycline-inducible MCT1 knockdown was reversed by integrating a constitutively active promoter with a MCT1 open reading frame (ORF) (MCT1 ORF_c), resulting in the Mia Paca-2 MCT1 KD_i + MCT1 ORF_c stable cell line (*SI Appendix*, Fig. S5*B*). An NTC was also generated using a nontargeting sequence (NTC ORF_c), resulting in the Mia Paca-2 MCT1 KD_i + NTC ORF_c stable cell line. At baseline, in the absence of doxycycline, stable cells with MCT1 KD_i + MCT1 ORF_c demonstrated increased MCT1 mRNA (*SI Appendix*, Fig. S5*G*) and membrane-bound MCT1 protein (Fig. 3*E*) compared with control MCT1 KD_i + NTC ORF_c cells. Consistently, doxycycline-free Mia Paca-2 KD_i + MCT1 ORF_c cells constitutively overexpressing MCT1 showed ∼130% significant increase in hyperpolarized [1-^{13}C]pyruvate-to-[1-^{13}C]lactate conversion rate compared with their MCT1 KD_i + NTC ORF_c control cells (Fig. 3*F*). In contrast, doxycycline-induced MCT1 knockdown cells, Mia Paca-2 MCT1 KD_i + NTC ORF_c, demonstrated ∼60% significant decrease in hyperpolarized [1-^{13}C]pyruvate-to-[1-^{13}C]lactate conversion rates compared with their doxycycline-free control cells (Fig. 3*G*). Furthermore, the doxycycline-induced MCT1 shRNA knockdown was rescued by cDNA in Mia Paca-2 stable cells with MCT1 KD_i + MCT1 ORF_c, resulting in an ∼fourfold significant increase in hyperpolarized [1-^{13}C]pyruvate-to-[1-^{13}C]lactate conversion rates (Fig. 3*G*). As a control, because [1-^{13}C]pyruvate-to-[1-^{13}C]lactate conversion through LDHA is coupled to NADH to NAD^+ oxidation, we examined NAD^+/NADH ratios across Mia Paca-2 NTC_i, Mia Paca-2 MCT1 KD_i, Mia Paca-2 MCT1 KD_i + NTC ORF_c, and Mia Paca-2 MCT1 KD_i + MCT1 ORF_c cells with and without doxycycline, simulating MCT1 knockdown, overexpression, and rescue conditions. No differences were observed in the NAD^+/NADH ratios across the tested stable cell lines (Fig. 3 *H* and *I*).

To validate the rate-limiting contribution of MCT1 to the apparent [1-^{13}C]pyruvate-to-[1-^{13}C]lactate conversion rates in another cell line, we stably overexpressed MCT1 in QGP1 cells, a

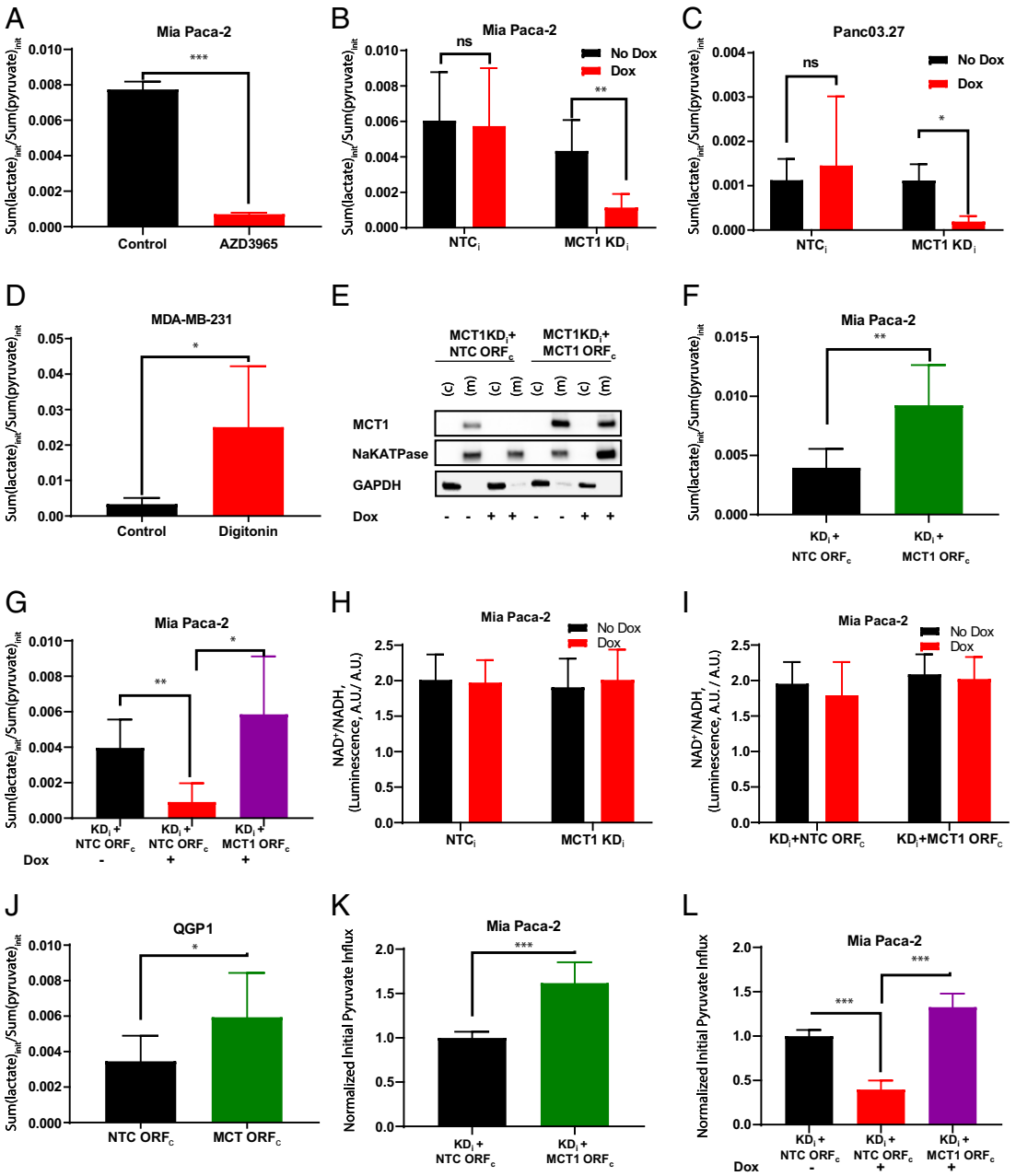

Fig. 3. The initial hyperpolarized [1-^{13}C]pyruvate-to-[1-^{13}C]lactate conversion rates in response to MCT1 modulation. (*A*) Pharmacological inhibition of MCT1 using 0.5 μM AZD3965. Initial hyperpolarized [1-^{13}C]pyruvate-to-[1-^{13}C]lactate conversion rates were calculated for without (black) and with (red) 0.5 μM AZD3965 pretreatment in Mia Paca2 cells. (*B* and *C*) Genetic knockdown of MCT1 in Mia Paca-2 (*B*) and Panc03.27 (*C*) cells; initial hyperpolarized [1-^{13}C]pyruvate-to-[1-^{13}C]lactate conversion rate in doxycycline-free control (black) or doxycycline-treated (red) stable cell lines transduced with NTC$_i$ or MCT1 KD$_i$ constructs. (*D*) Permeabilization of MDA-MB-231 cells with digitonin; the initial hyperpolarized [1-^{13}C]pyruvate-to-[1-^{13}C]lactate conversion rate in MDA-MB-231 cells without digitonin treatment as control (black) or with digitonin treatment for membrane permeabilization (red). (*E*) Western blot of doxycycline-inducible MCT1 knockdown Mia Paca-2 MCT1 KD$_i$ cells containing a constitutive NTC ORF$_c$ or MCT1 ORF$_c$. (*F*) Overexpression of MCT1 in Mia Paca-2 MCT1 KD$_i$ cells; the initial hyperpolarized [1-^{13}C]pyruvate-to-[1-^{13}C]lactate conversion rates of Mia Paca-2 stable cell lines with two vectors, KD$_i$ + NTC ORF$_c$ (black) or KD$_i$ + MCT1 ORF$_c$ (green), without doxycycline induction. (*G*) Genetic rescue of MCT1 in Mia Paca-2 MCT1 KD$_i$ cells with MCT1 overexpression ORF$_c$; the initial hyperpolarized [1-^{13}C]pyruvate-to-[1-^{13}C]lactate conversion rates of Mia Paca-2 stable cell lines with two vectors, KD$_i$ + NTC ORF$_c$ or KD$_i$ + MCT1 ORF$_c$, with and without doxycycline induction. KD$_i$ + NTC$_c$ without doxycycline serves as the control (black). KD$_i$ + NTC$_c$ with doxycycline (red) induces MCT1 knockdown compared with the control. KD$_i$ + MCT1 ORF$_c$ with doxycycline (purple) demonstrates doxycycline-inducible knockdown of endogenous MCT1 rescued by the constitutively overexpressing MCT1 ORF$_c$. (*H*) NAD$^+$/NADH ratios of Mia Paca-2 NTC$_i$ and Mia Paca-2 MCT1 KD$_i$ with/without doxycycline induction. (*I*) NAD$^+$/NADH ratios of Mia Paca-2 KD$_i$ + NTC ORF$_c$ and Mia Paca-2 KD$_i$ + MCT1 ORF$_c$ with/without doxycycline induction. (*J*) Overexpression of MCT1 in QGP1 cells; the initial hyperpolarized [1-^{13}C]pyruvate-to-[1-^{13}C]lactate conversion rates of the QGP1 stable cell line with NTC ORF$_c$ (black) or MCT1 ORF$_c$ (green), which constitutively overexpresses MCT1 protein. (*K*) Changes of initial pyruvate influx rates (6 s) in Mia Paca-2 stable cell lines with two vectors, KD$_i$ + NTC ORF$_c$ (black) or KD$_i$ + MCT1 ORF$_c$ (green) without doxycycline induction. Initial pyruvate influx values are normalized to KD$_i$ + NTC ORF$_c$ control. (*L*) Changes of initial pyruvate influx rates (6 s) in Mia Paca-2 MCT1 KD$_i$ cells with MCT1 overexpression ORF$_c$ or NTC ORF$_c$. Initial pyruvate influx values are normalized to KD$_i$ + NTC ORF$_c$ control. (*F*). Error bars represent SD. *$P < 0.05$; **$P < 0.01$, ***$P < 0.0001$ (paired *t* test). A.U., arbitrary units; ns, not significant.

cell line with low basal MCT1, by integrating a MCT1 ORF_c (*SI Appendix*, Fig. S5*B*), and membrane-bound MCT1 protein overexpression was confirmed at both transcriptional and protein levels (*SI Appendix*, Fig. S5 *H* and *I*). Similar to Mia Paca2 MCT1 overexpression, initial [1-^{13}C]pyruvate-to-[1-^{13}C]lactate conversion rates showed a significant increase of ∼50% in QGP1 cells with MCT1 overexpression (MCT1 ORF_c) compared with the NTC (NTC ORF_c) (Fig. 3*J*). These data demonstrated that the conversion of [1-^{13}C]pyruvate-to-[1-^{13}C]lactate was dependent and rate-limited by MCT1 expression and not LDHA activity. Furthermore, the initial pyruvate influxes in Mia Paca-2 MCT1 KD_i + NTC ORF_c, and Mia Paca-2 MCT1 KD_i + MCT1 ORF_c stable

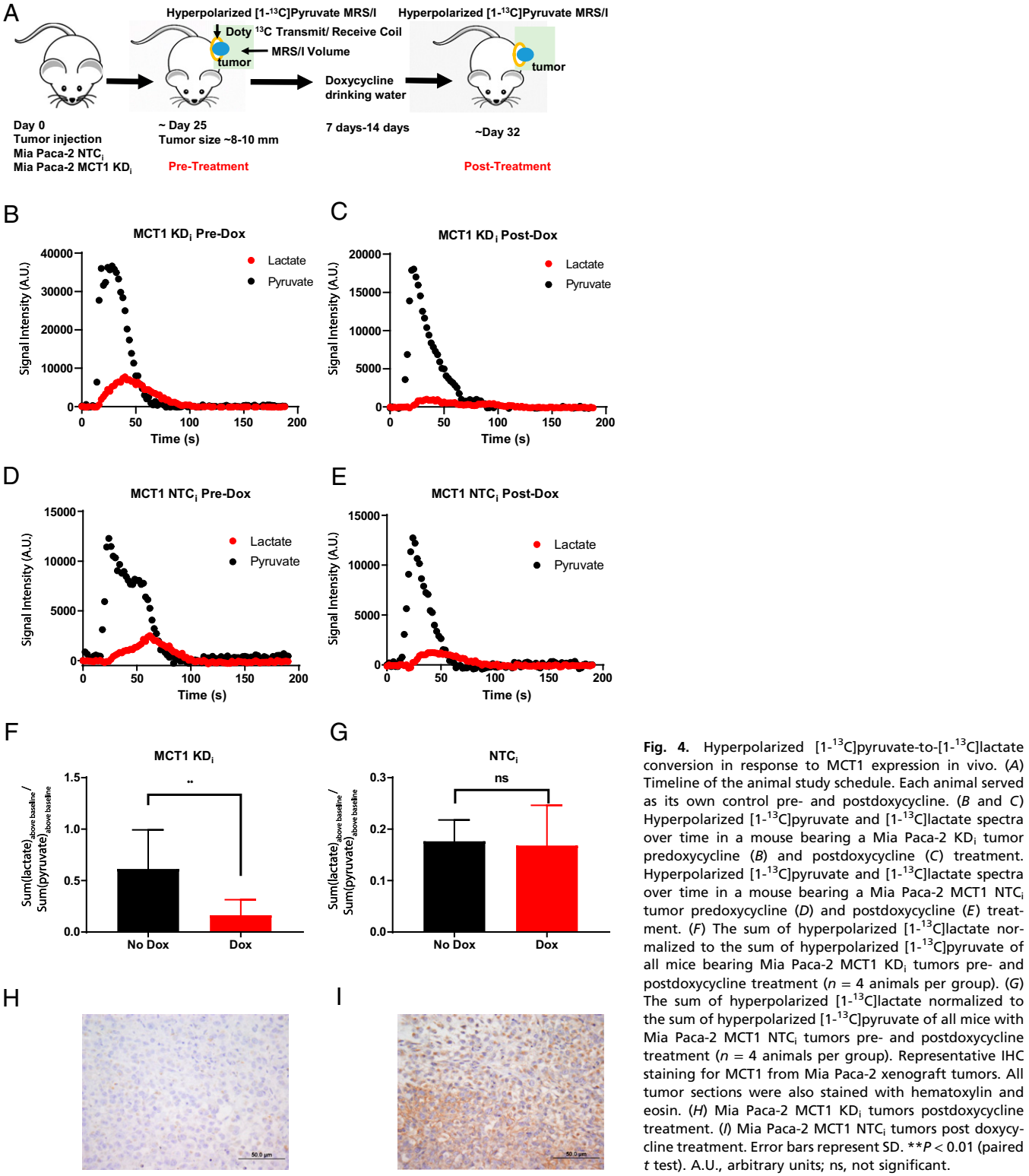

Fig. 4. Hyperpolarized [1-^{13}C]pyruvate-to-[1-^{13}C]lactate conversion in response to MCT1 expression in vivo. (*A*) Timeline of the animal study schedule. Each animal served as its own control pre- and postdoxycycline. (*B* and *C*) Hyperpolarized [1-^{13}C]pyruvate and [1-^{13}C]lactate spectra over time in a mouse bearing a Mia Paca-2 KD_i tumor predoxycycline (*B*) and postdoxycycline (*C*) treatment. Hyperpolarized [1-^{13}C]pyruvate and [1-^{13}C]lactate spectra over time in a mouse bearing a Mia Paca-2 MCT1 NTC_i tumor predoxycycline (*D*) and postdoxycycline (*E*) treatment. (*F*) The sum of hyperpolarized [1-^{13}C]lactate normalized to the sum of hyperpolarized [1-^{13}C]pyruvate of all mice bearing Mia Paca-2 MCT1 KD_i tumors pre- and postdoxycycline treatment ($n = 4$ animals per group). (*G*) The sum of hyperpolarized [1-^{13}C]lactate normalized to the sum of hyperpolarized [1-^{13}C]pyruvate of all mice with Mia Paca-2 MCT1 NTC_i tumors pre- and postdoxycycline treatment ($n = 4$ animals per group). Representative IHC staining for MCT1 from Mia Paca-2 xenograft tumors. All tumor sections were also stained with hematoxylin and eosin. (*H*) Mia Paca-2 MCT1 KD_i tumors postdoxycycline treatment. (*I*) Mia Paca-2 MCT1 NTC_i tumors post doxycycline treatment. Error bars represent SD. $^{**}P < 0.01$ (paired *t* test). A.U., arbitrary units; ns, not significant.

cells were also evaluated (Fig. 3 *K* and *L*). Once again, the initial unidirectional pyruvate influx mediated by MCT1 was tightly correlated with the observed hyperpolarized [1-^{13}C]pyruvate-to-[1-^{13}C]lactate conversion rates (Fig. 3 *F* and *G*).

Hyperpolarized [1-^{13}C]Pyruvate-to-[1-^{13}C]Lactate Conversion Rates Are Dependent on MCT1 Expression in Living Animals. With the observed dependence of hyperpolarized [1-^{13}C]pyruvate-to-[1-^{13}C]lactate conversion rates on membrane-localized MCT1 in live cells, the contribution of MCT1 in vivo was examined using hyperpolarized [1-^{13}C]pyruvate in live animal tumor models (Fig. 4*A*). Subcutaneous tumor models of Mia Paca-2 cells stably expressing either the doxycycline-inducible MCT1 KD_i or an NTC_i sequence were used. Once tumors reached ∼8 mm in diameter, an initial hyperpolarized [1-^{13}C]pyruvate MRSI dataset was acquired. All animals were then administered 1 mg/mL doxycycline + 5% fructose for ∼7 to 14 d to induce either the targeted MCT1 KD_i shRNA or NTC_i shRNA. A posttreatment MRSI image was then acquired in the same animals. The spectra of hyperpolarized [1-^{13}C]pyruvate and [1-^{13}C]lactate was integrated over an ∼3-min period for mice with either Mia Paca-2 MCT1 KD_i shRNA (Fig. 4 *B* and *C*) or Mia Paca-2 NTC_i shRNA (Fig. 4 *D* and *E*) pre- and postdoxycycline induction. The sum of [1-^{13}C]lactate-to-[1-^{13}C]pyruvate ratios above baseline over time were calculated instead of the previously used initial [1-^{13}C]lactate-to-[1-^{13}C]pyruvate ratios due to decreased signal-to-noise ratios in vivo. Comparing the pre- and postdoxycycline MRSI data, hyperpolarized [1-^{13}C]pyruvate-to-[1-^{13}C]lactate conversion was significantly decreased by ∼70% only in animals with tumors stably expressing MCT1 KD_i (Fig. 4*F*). In contrast, hyperpolarized [1-^{13}C]pyruvate-to-[1-^{13}C]lactate conversion was not significantly different in the NTC group (Fig. 4*G*). In vivo doxycycline-inducible knockdown of MCT1 or NTC were confirmed by immunohistochemistry (IHC) staining of MCT1 at the endpoint (Fig. 4 *H* and *I* and *SI Appendix*, Fig. S6 *A–F*). Overall, these data strongly supported the MCT1 dependency of the apparent hyperpolarized [1-^{13}C]pyruvate-to-[1-^{13}C]lactate conversion ratio in vivo.

Clinical Relevance of Pyruvate Transporters. Overall, data indicated that hyperpolarized [1-^{13}C]pyruvate MRSI was a functional biomarker of MCT1 transport activity in tumors in vivo. Thus, to explore the potential clinical relevance of MCTs, we compared expression profiles of MCT family members MCT1, -2, and -4 in datasets from the HPA, across various tissues derived from both normal individuals and cancer patients (*SI Appendix*, Fig. S7 *A–C*). Overall, MCT1 and MCT4 were found to be overexpressed among many examined tumors relative to normal tissues (*SI Appendix*, Fig. S7 *A* and *C*). Kaplan–Meier survival analysis showed that patients with high expression of MCT1 or LDHA correlated with poor overall survival, of which four tumor types showed that both MCT1 and LDHA correlated with poor overall survival, including pancreatic (n = 176; overall survival: $P < 0.05$ and $P < 0.0001$, respectively; Fig. 5 *A* and *B*), renal (n = 877; overall survival: $P < 0.0001$ and $P < 0.0001$, respectively; Fig. 5 *D* and *E*), lung (n = 994; overall survival: $P < 0.05$ and $P < 0.0001$, respectively; *SI Appendix*, Fig. S7 *D* and *E*), and cervical (n = 291; overall survival: $P < 0.0001$ and $P < 0.001$, respectively; *SI Appendix*, Fig. S7 *G* and *H*) cancer patients. Because both MCT1 and LDHA are necessary to visualize hyperpolarized [1-^{13}C]pyruvate-to-[1-^{13}C]lactate conversion, hyperpolarized [1-^{13}C]pyruvate MRSI could potentially be used as a prognostic marker for patients with pancreatic, renal, lung, and cervical cancers. Furthermore, overall MCT1 expression profiles significantly correlated with LDHA expression profiles for pancreatic (r = 0.39, $P < 0.0001$; Fig. 5*C*), renal (r = 0.62, $P < 0.0001$; Fig. 5*F*), lung (r = 0.30, $P < 0.0001$; *SI Appendix*, Fig. S7*F*), and cervical (r = 0.44, $P < 0.0001$; *SI Appendix*, Fig. S7*I*) cancer patients. This could explain the previously identified correlation between hyperpolarized [1-^{13}C]pyruvate-to-[1-^{13}C]lactate conversion and LDHA (47, 48). However, because high MCT1 expression appears to be rate-limiting for the conversion of hyperpolarized [1-^{13}C]pyruvate-to-[1-^{13}C]lactate, hyperpolarized [1-^{13}C]pyruvate MRSI will strongly correlate with high LDHA expression only in those tumors concurrently overexpressing MCT1.

Discussion

Many preclinical and clinical studies utilizing hyperpolarized [1-^{13}C]pyruvate MRSI have observed that advanced tumor tissues exhibit increased [1-^{13}C]pyruvate-to-[1-^{13}C]lactate conversion rates (20, 24, 37), attributed to glycolysis or increased expression and activity of LDHA (47, 48). Clinically, tissues with low hyperpolarized [1-^{13}C]pyruvate-to-[1-^{13}C]lactate conversion rates are considered to be in a slower glycolytic flux state, aligning with nonaggressive or benign tumors, whereas tissues with high [1-^{13}C]pyruvate-to-[1-^{13}C]lactate conversion rates are considered to be in a high glycolytic flux state and more aggressive (49).

However, when systematically reexamining the fate of administrated hyperpolarized [1-^{13}C]pyruvate in vivo, the observed [1-^{13}C]pyruvate-to-[1-^{13}C]lactate conversion rates can be deconvolved into multiple steps. Intravenous administration of hyperpolarized [1-^{13}C]pyruvate first delivers the reagent to the vascular

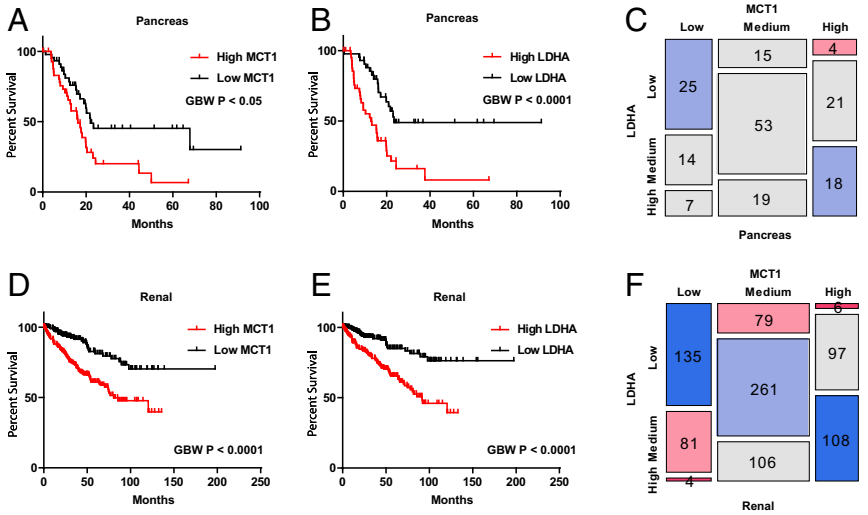

Fig. 5. mRNA expression profiles of MCT1 or LDHA correlated with overall patient survival in pancreatic and renal cancers. Gehan–Breslow–Wilcoxon tests were used to estimate the *P* values between high- and low-expression groups (using the top and bottom 25% as the cutoff for grouping). Pearson χ^2 tests were used to estimate the *P* values between MCT1 and LDHA expression. (*A* and *B*) Kaplan–Meier survival analysis in pancreatic cancer patients (n = 176) indicates that high MCT1 or LDHA expression correlates with poorer patient survival. (*A*) MCT1 ($P < 0.05$). (*B*) LDHA ($P < 0.0001$). (*C*) Mosaic plot in pancreatic cancer patients indicates that MCT1 expression correlates with LDHA expression ($P < 0.0001$). (*D* and *E*) Kaplan–Meier survival analysis in renal cancer patients (n = 877) indicates that high MCT1 or LDHA expression correlates with poorer patient survival. (*D*) MCT1 ($P < 0.0001$). (*E*) LDHA ($P < 0.0001$). (*F*) Mosaic plot in renal cancer patients indicates that MCT1 expression correlates with LDHA expression ($P < 0.0001$).

and extracellular spaces. As a charged molecule, hyperpolarized [1-^{13}C]pyruvate cannot freely diffuse across the plasma membrane of a cell. Consequently, for a hyperpolarized [1-^{13}C]pyruvate molecule to be reduced to lactate via LDHA (a cytoplasmic enzyme), [1-^{13}C]pyruvate first must be transported into cells. Proton-coupled MCTs located on plasma membranes are physiologically involved in pyruvate influx (50), with the most ubiquitously expressed pyruvate transporter in the MCT family being MCT1, while MCT2 is the most efficient pyruvate transporter (32). Contradictory preclinical reports of whether hyperpolarized [1-^{13}C]pyruvate transmembrane transport is rate-limiting have been published. For example, using various concentrations of hyperpolarized [1-^{13}C]pyruvate, Harris et al. (34) modeled the kinetics of hyperpolarized [1-^{13}C]pyruvate transport with a K_m = 2.14 mM, concluding that MCT1 is the rate-limiting step for a human breast cancer cell line. By contrast, Witney et al. (35) performed cell-permeabilization experiments using murine lymphoma (EL-4) cells suggesting that MCT1 is not the rate-limiting step for hyperpolarized [1-^{13}C]pyruvate-to-[1-^{13}C]lactate conversion rates, as observed by hyperpolarized MRSI. In addition, the contribution of MCT4 and lactate export was shown to correlate with [1-^{13}C]pyruvate-to-[1-^{13}C]lactate conversion rates in a renal cell carcinoma cell line (51). Regardless, most studies in preclinical models attribute the observed [1-^{13}C]pyruvate-to-[1-^{13}C]lactate conversion rates (or ratios) to LDHA activity or report the correlation with LDHA (28, 30, 52), while most clinical studies conventionally correlate the [1-^{13}C]pyruvate-to-[1-^{13}C]lactate conversion with LDHA activity (37). However, in a recently published [1-^{13}C]pyruvate MRSI clinical study in prostate cancer patients, Granlund et al. (36) found that elevated hyperpolarized [1-^{13}C]lactate correlated with the assigned high Gleason scores ($P \leq 0.0001$), and, furthermore, immunohistochemical staining of patient samples suggested that enhanced hyperpolarized [1-^{13}C]lactate correlated with MCT1. In addition, Gallagher et al. (39) recently reported that [1-^{13}C]pyruvate-to-[1-^{13}C]lactate conversion correlated with pyruvate transporter expression and hypoxia-inducible factor 1 (HIF1α) but not LDHA. While high quality and provocative, these clinical correlates lack the mechanistic rigor for establishment of causation.

Herein, to rigorously address this fundamental question as to signal source, we used genetically engineered tumor cells with inducible vectors to knock down or overexpress MCT1 in a panel of tumor cells that sampled the relevant metabolic space. Our data demonstrated that the observed hyperpolarized [1-^{13}C]pyruvate-to-[1-^{13}C]lactate conversion rates were neither dependent nor rate-limited by cellular glycolysis, LDHA protein levels, LDHA activities, intracellular pyruvate, or lactate, but rather by pyruvate influx mediated by MCT proteins localized to the plasma membrane. Contrary to standard models, we identified that hyperpolarized [1-^{13}C]pyruvate-to-[1-^{13}C]lactate conversion rates were negatively correlated with LDHA total protein and enzyme activities across a panel of cell lines. Note that at the level of RNA in clinical samples, MCT1 expression profiles significantly correlated with LDHA expression profiles among selected cancers, and, therefore, the observed apparent correlation between [1-^{13}C]pyruvate-to-[1-^{13}C]lactate conversion and LDHA activity could be accounted for by the cocorrelation between LDHA and MCT1 expression. In contrast, for cell lines and tumors where LDHA expression does not positively correlate with MCT1 expression, [1-^{13}C]pyruvate-to-[1-^{13}C]lactate conversion rates would not reflect LDHA activities, which could explain the discrepancies between many previously reported results.

Mechanistically, data indicated that the conversion of hyperpolarized [1-^{13}C]pyruvate to [1-^{13}C]lactate was rate-limited by MCT1. Importantly, in this context, hyperpolarized [1-^{13}C]pyruvate MRSI is a dynamic assessment of overall net transport activity mediated by MCT1 in vivo, which is a function of the number of MCT1 transporter proteins properly inserted into the plasma membrane multiplied by their specific activity (turnover kinetics), the latter dependent on the specific biochemical details of the protein and microenvironment (K_m, V_{max}, local substrate concentrations). For example, increases in conversion rates would not be expected to be directly proportional to increases of MCT1 protein levels in nonsaturating conditions. Furthermore, note that ancillary proteins including basigin/CD147 and embigin/gp70 are required for translocation of MCTs to the plasma membrane (32). When MCTs are overexpressed in the absence of these ancillary proteins, MCTs could fail to reach the plasma membrane due to saturation of the pool of ancillary proteins (46). Besides turnover kinetics, these ancillary proteins could also explain why increases in [1-^{13}C]lactate production were directionally consistent but less than the proportional increases in MCT1 content at higher expression levels, as observed across the cell panel in our study.

As shown in the schematic diagram (Fig. 1*A*), pyruvate bulk delivery/perfusion, pyruvate influx, LDHA activity, intracellular pyruvate concentration, intracellular lactate concentration, and NADH/NAD$^+$ in principle could all affect the apparent kinetics of hyperpolarized [1-^{13}C]pyruvate-to-[1-^{13}C]lactate conversion. Assuming bulk perfusion and vascular delivery of the injected hyperpolarized [1-^{13}C]pyruvate, we find that the influx of exogenous pyruvate mediated by MCT1 is the rate-limiting step of this entire conversion process. Only when MCT1 is massively overexpressed, then other downstream factors, including LDHA activity, NADH, intracellular pyruvate, and lactate could in theory rate-limit [1-^{13}C]lactate production. We found no significant correlation between intracellular lactate content and hyperpolarized [1-^{13}C]pyruvate-to-[1-^{13}C]lactate conversion across the cell panel, consistent with several previous metabolomics studies that demonstrated that lactate pools do not correlate with hyperpolarized [1-^{13}C]lactate production (53, 54). However, defining MCT1 as the rate-limiting step also provides an additional mechanism for some observations that a large pool of endogenous intracellular lactate can indeed drive the observed conversion of [1-^{13}C]pyruvate to [1-^{13}C]lactate (7), attributed in principle to the dilution of labeled [1-^{13}C]lactate, thereby diminishing LDHA-mediated back-reactions. In this regard, recent biophysical analysis has demonstrated that turnover kinetics of monocarboxylate transporters operating in pyruvate/lactate exchange mode are significantly faster than turnover kinetics when operating in unidirectional proton-coupled cotransport mode (55, 56). Thus, the presence of high intracellular lactate will promote rapid MCT1-mediated exchange with extracellular [1-^{13}C]pyruvate during a hyperpolarized [1-^{13}C]pyruvate MRSI experiment, driving influx of [1-^{13}C]pyruvate and enhancing substrate presentation to LDHA for [1-^{13}C]pyruvate-to-[1-^{13}C]lactate conversion.

MDA-MB-231 tumors, high in LDHA but low in MCT1 expression, are important to highlight and portend the risk of clinical false-negative interrogation of tumors with hyperpolarized [1-^{13}C]pyruvate. If hyperpolarized [1-^{13}C]pyruvate-to-[1-^{13}C]lactate conversion rates always correlated with tumor aggressiveness and high LDHA, then MDA-MB-231, a known aggressive triple-negative breast tumor, should have demonstrated high [1-^{13}C]pyruvate-to-[1-^{13}C]lactate conversion rates; similarly for QGP1, a pancreatic neuroendocrine tumor. However, the hyperpolarized [1-^{13}C]pyruvate MRS signals for these two remarkably MCT1-low tumors showed low [1-^{13}C]pyruvate-to-[1-^{13}C]lactate conversion rates, indistinguishable from control HPNE cells, which would be potentially problematic clinically.

The expression of MCT1 and LDHA vary due to tumor heterogeneity, and, thus, baseline hyperpolarized [1-^{13}C]lactate conversion could fluctuate within the tumor cell population. Consequently, it could be challenging to use baseline measurements of hyperpolarized [1-^{13}C]pyruvate-to-[1-^{13}C]lactate conversion rates to differentiate tumor from normal tissues. However, changes between hyperpolarized [1-^{13}C]pyruvate MRSI in the same patient pre- and post-response to therapy could be informative in

principle, especially given an expectation that MCT1 is a potential prognostic marker (24, 57). Consistent with the genomic profiling results, Dong et al. (24) reported that hyperpolarized [1-^{13}C]pyruvate could predict treatment response to mTOR inhibitors in patient-derived renal cell carcinoma xenograft models. In addition, it has been reported that hyperpolarized [1-^{13}C]pyruvate MRSI can detect and monitor progression of advanced pancreatic preneoplasia (57). Also, when MCT1 is known to be overexpressed and not rate-limiting in a particular cancer, [1-^{13}C]pyruvate may have potential as a biomarker for LDHA in such special cases. In addition, hyperpolarized [1-^{13}C]pyruvate MRSI could be used to monitor therapeutic responses to LDHA or glycolysis inhibitors by comparing pre- and posttreatment [1-^{13}C]pyruvate-to-[1-^{13}C]lactate conversion rates assuming that the therapy does not directly target MCTs nor induce compensatory changes in MCT expression or membrane localization. Preclinical studies have reported that decreased hyperpolarized [1-^{13}C]lactate production posttherapy correlated with enhanced responses (26, 58). Furthermore, MCT1 inhibitors have demonstrated anticancer therapeutic effects in preclinical breast cancer models (59). An MCT1/2 inhibitor, AZD3965, is currently undergoing phase I/II clinical trials as an anticancer therapeutic for prostate cancer, gastric cancer, and diffuse large B cell lymphoma (60, 61). In this context, hyperpolarized [1-^{13}C]pyruvate would be a potential pharmacodynamic biomarker to study the efficacy of MCT inhibitors. Moreover, due to metabolic heterogeneity, melanoma cells with high MCT1 have been reported to have high metastatic potential compared with their low-MCT1 counterparts (62). Having identified that the hyperpolarized [1-^{13}C]pyruvate-to-[1-^{13}C]lactate conversion rate primarily measures MCT1-mediated [1-^{13}C]pyruvate influx, hyperpolarized [1-^{13}C]pyruvate MRSI can be a potential imaging biomarker for evaluating melanoma metastatic potential.

MCT1 expression has been identified as a prognostic biomarker for lung and endometrial cancers (63, 64). Moreover, MCT1 overexpression is associated with poor prognosis for several cancers, including glioma, renal, pancreatic, and cervical cancers (65–68). Cancers tend to overexpress MCT1 to facilitate monocarboxylate transport, including pyruvate and lactate influx and efflux (59), while MCT4 has been reported to support lactate export, facilitating tumor growth, and renal carcinoma metastasis (51, 64, 69). For the clinical translation of hyperpolarized [1-^{13}C]pyruvate MRSI, the appearance of hyperpolarized [1-^{13}C]lactate signal requires, at the minimum, the expression of both MCT1 and LDHA. Hyperpolarized [1-^{13}C]pyruvate MRSI could therefore be used as a noninvasive metabolic-imaging modality for functional assessment of MCT1 as a prognostic marker in these patient populations. Furthermore, preclinical studies have shown that hyperpolarized [1-^{13}C]pyruvate MRSI could further be linked to therapeutic response (70). Since hyperpolarized [1-^{13}C]lactate detection requires both [1-^{13}C]pyruvate influx mediated by MCTs, primarily MCT1, as well as LDHA-catalyzed hyperpolarized [1-^{13}C]pyruvate-to-[1-^{13}C]lactate conversion, in theory, hyperpolarized [1-^{13}C]pyruvate MRSI has the potential to be used as a prognostic imaging biomarker that predicts cancer prognosis, for which both high MCT1 and LDHA activity correlate with poor overall patient survival.

Overall, our data indicate that hyperpolarized [1-^{13}C]pyruvate-to-[1-^{13}C]lactate conversion is not a direct measure of LDHA activity nor nonoxidative glycolysis. In effect, LDHA activity enables the intracellular pool of [1-^{13}C]pyruvate to be distinguished from extracellular [1-^{13}C]pyruvate by the appearance of the product [1-^{13}C]lactate, an obligatory intracellular metabolite in this context. When interpreting hyperpolarized [1-^{13}C]pyruvate MRSI results, our data indicate that the capacity to observe hyperpolarized [1-^{13}C]pyruvate-to-[1-^{13}C]lactate conversion rates are primarily dependent on and rate-limited by MCT activity, especially MCT1. To the degree that MCT1 function is linked to poor survival in selected cancers, hyperpolarized MRSI may still fill an unmet need for a noninvasive marker of prognosis and functional monitoring of therapeutic response through imaging.

Data Availability. All study data are included in the article and *SI Appendix*.

ACKNOWLEDGMENTS. This study was funded by NIH Grant P50 CA94056 to the MD Anderson Cancer Center–Washington University Inter-Institutional Molecular Imaging Center; the Gerald Dewey Dodd, Jr., Endowed Distinguished Chair of the University of Texas MD Anderson Cancer Center; a faculty University of Texas Science and Technology Acquisition and Retention Award; a grant from the Pancreatic Cancer Action Network (16-65-BHAT); Cancer Prevention and Research Institute of Texas Research Training Grant Award RP170067; and a generous gift from the Estate of Barbara Cox Anthony/Koch Foundation. We thank the Biostatistics Resource and the Small Animal Imaging Facility of the MD Anderson Cancer Center for animal imaging assistance, especially Charles Kingsley, Jorge Delacerda, Jim Bankson, Gary Martinez, and Christopher Walker. The Biostatistics Resource and the Small Animal Imaging Facility obtain support from NCI Cancer Center Support Grant P30 CA016672.

1. D. Hanahan, R. A. Weinberg, Hallmarks of cancer: The next generation. *Cell* **144**, 646–674 (2011).
2. R. J. DeBerardinis, N. S. Chandel, Fundamentals of cancer metabolism. *Sci. Adv.* **2**, e1600200 (2016).
3. R. J. DeBerardinis, J. J. Lum, G. Hatzivassiliou, C. B. Thompson, The biology of cancer: Metabolic reprogramming fuels cell growth and proliferation. *Cell Metab.* **7**, 11–20 (2008).
4. N. N. Pavlova, C. B. Thompson, The emerging hallmarks of cancer metabolism. *Cell Metab.* **23**, 27–47 (2016).
5. H. Shim *et al.*, c-Myc transactivation of LDH-A: implications for tumor metabolism and growth. *Proc. Natl. Acad. Sci. U.S.A.* **94**, 6658–6663 (1997).
6. M. G. Vander Heiden, L. C. Cantley, C. B. Thompson, Understanding the warburg effect: The metabolic requirements of cell proliferation. *Science* **324**, 1029–1033 (2009).
7. S. E. Day *et al.*, Detecting tumor response to treatment using hyperpolarized 13C magnetic resonance imaging and spectroscopy. *Nat. Med.* **13**, 1382–1387 (2007).
8. S. Hu *et al.*, 13C-pyruvate imaging reveals alterations in glycolysis that precede c-Myc-induced tumor formation and regression. *Cell Metab.* **14**, 131–142 (2011).
9. C. S. Ward *et al.*, Noninvasive detection of target modulation following phosphatidylinositol 3-kinase inhibition using hyperpolarized 13C magnetic resonance spectroscopy. *Cancer Res.* **70**, 1296–1305 (2010).
10. V. Di Gialleonardo, D. M. Wilson, K. R. Keshari, The potential of metabolic imaging. *Semin. Nucl. Med.* **46**, 28–39 (2016).
11. A. Zhu, D. Lee, H. Shim, Metabolic positron emission tomography imaging in cancer detection and therapy response. *Semin. Oncol.* **38**, 55–69 (2011).
12. A. R. Pantel, D. Ackerman, S. C. Lee, D. A. Mankoff, T. P. Gade, Imaging cancer metabolism: Underlying biology and emerging strategies. *J. Nucl. Med.* **59**, 1340–1349 (2018).
13. A. Almuhaideb, N. Papathanasiou, J. Bomanji, 18F-FDG PET/CT imaging in oncology. *Ann. Saudi Med.* **31**, 3–13 (2011).
14. J. H. Ardenkjaer-Larsen *et al.*, Increase in signal-to-noise ratio of > 10,000 times in liquid-state NMR. *Proc. Natl. Acad. Sci. U.S.A.* **100**, 10158–10163 (2003).
15. K. M. Brindle, S. E. Bohndiek, F. A. Gallagher, M. I. Kettunen, Tumor imaging using hyperpolarized 13C magnetic resonance spectroscopy. *Magn. Reson. Med.* **66**, 505–519 (2011).
16. C. Guglielmetti *et al.*, Hyperpolarized ^{13}C MR metabolic imaging can detect neuroinflammation in vivo in a multiple sclerosis murine model. *Proc. Natl. Acad. Sci. U.S.A.* **114**, E6982–E6991 (2017).
17. V. Z. Miloushev *et al.*, Hyperpolarized ^{13}C pyruvate mouse brain metabolism with absorptive-mode EPSI at 1T. *J. Magn. Reson.* **275**, 120–126 (2017).
18. V. Z. Miloushev *et al.*, Metabolic imaging of the human brain with hyperpolarized (13)C pyruvate demonstrates (13)C lactate production in brain tumor patients. *Cancer Res.* **78**, 3755–3760 (2018).
19. T. B. Rodrigues *et al.*, Magnetic resonance imaging of tumor glycolysis using hyperpolarized 13C-labeled glucose. *Nat. Med.* **20**, 93–97 (2014).
20. E. M. Serrao, K. M. Brindle, Potential clinical roles for metabolic imaging with hyperpolarized [1-(13)C]pyruvate. *Front. Oncol.* **6**, 59 (2016).
21. P. Bhattacharya, B. D. Ross, R. Bünger, Cardiovascular applications of hyperpolarized contrast media and metabolic tracers. *Exp. Biol. Med. (Maywood)* **234**, 1395–1416 (2009).
22. P. Dutta *et al.*, Assessing therapeutic efficacy in real-time by hyperpolarized magnetic resonance metabolic imaging. *Cells* **8**, E340 (2019).
23. Z. J. Wang *et al.*, Hyperpolarized (13)C MRI: State of the art and future directions. *Radiology* **291**, 273–284 (2019).
24. Y. Dong *et al.*, Hyperpolarized MRI visualizes warburg effects and predicts treatment response to mTOR Inhibitors in patient-derived ccRCC xenograft models. *Cancer Res.* **79**, 242–250 (2019).

25. K. Golman, R. I. Zandt, M. Lerche, R. Pehrson, J. H. Ardenkjaer-Larsen, Metabolic imaging by hyperpolarized 13C magnetic resonance imaging for in vivo tumor diagnosis. *Cancer Res.* **66**, 10855–10860 (2006).
26. B. T. Scroggins *et al*., Hyperpolarized [1-(13)C]-pyruvate magnetic resonance spectroscopic imaging of prostate cancer in vivo predicts efficacy of targeting the Warburg effect. *Clin. Cancer Res.* **24**, 3137–3148 (2018).
27. A. E. Hansen *et al*., Combined hyperpolarized ^{13}C-pyruvate MRS and ^{18}F-FDG PET (hyperPET) estimates of glycolysis in canine cancer patients. *Eur. J. Radiol.* **103**, 6–12 (2018).
28. Y. Adler-Levy *et al*., In-cell determination of lactate dehydrogenase activity in a luminal breast cancer model (-) ex vivo investigation of excised xenograft tumor slices using dDNP hyperpolarized [1-(13)C]pyruvate. *Sensors (Basel)* **19**, E2089 (2019).
29. D. K. Hill *et al*., ^{1}H NMR and hyperpolarized ^{13}C NMR assays of pyruvate-lactate: A comparative study. *NMR Biomed.* **26**, 1321–1325 (2013).
30. N. Lev-Cohain *et al*., Real-time ALT and LDH activities determined in viable precision-cut mouse liver slices using hyperpolarized [1-^{13} C]pyruvate-Implications for studies on biopsied liver tissues. *NMR Biomed.* **32**, e4043 (2019).
31. K. Saito *et al*., 13C-MR spectroscopic imaging with hyperpolarized [1-13C]pyruvate detects early response to radiotherapy in SCC tumors and HT-29 tumors. *Clin. Cancer Res.* **21**, 5073–5081 (2015).
32. J. Pérez-Escuredo *et al*., Monocarboxylate transporters in the brain and in cancer. *Biochim. Biophys. Acta* **1863**, 2481–2497 (2016).
33. M. E. Morris, M. A. Felmlee, Overview of the proton-coupled MCT (SLC16A) family of transporters: Characterization, function and role in the transport of the drug of abuse gamma-hydroxybutyric acid. *AAPS J.* **10**, 311–321 (2008).
34. T. Harris, G. Eliyahu, L. Frydman, H. Degani, Kinetics of hyperpolarized 13C1-pyruvate transport and metabolism in living human breast cancer cells. *Proc. Natl. Acad. Sci. U.S.A.* **106**, 18131–18136 (2009).
35. T. H. Witney, M. I. Kettunen, K. M. Brindle, Kinetic modeling of hyperpolarized 13C label exchange between pyruvate and lactate in tumor cells. *J. Biol. Chem.* **286**, 24572–24580 (2011).
36. K. L. Granlund *et al*., Hyperpolarized MRI of human prostate cancer reveals increased lactate with tumor grade driven by monocarboxylate transporter 1. *Cell Metab.* **31**, 105–114.e3 (2020).
37. S. J. Nelson *et al*., Metabolic imaging of patients with prostate cancer using hyperpolarized [1-(1)(3)C]pyruvate. *Sci. Transl. Med.* **5**, 198ra108 (2013).
38. T. Delgado-Goni *et al*., The BRAF inhibitor vemurafenib activates mitochondrial metabolism and inhibits hyperpolarized pyruvate-lactate exchange in BRAF-mutant human melanoma cells. *Mol. Cancer Ther.* **15**, 2987–2999 (2016).
39. F. A. Gallagher *et al*., Imaging breast cancer using hyperpolarized carbon-13 MRI. *Proc. Natl. Acad. Sci. U.S.A.* **117**, 2092–2098 (2020).
40. N. M. Zacharias *et al*., Assessing metabolic intervention with a glutaminase inhibitor in real-time by hyperpolarized magnetic resonance in acute myeloid leukemia. *Mol. Cancer Ther.* **18**, 1937–1946 (2019).
41. J. J. Miller *et al*., (13)C pyruvate transport across the blood-brain barrier in preclinical hyperpolarised MRI. *Sci. Rep.* **8**, 15082 (2018).
42. J. Y. Park *et al*., Development of suspension cell culture model to mimic circulating tumor cells. *Oncotarget* **9**, 622–640 (2017).
43. T. Andersen, P. Auk-Emblem, M. Dornish, 3D cell culture in alginate hydrogels. *Microarrays (Basel)* **4**, 133–161 (2015).
44. B. G. Berman, M. L. Halperin, Effect of insulin on pyruvate metabolism in epididymal adipose tissue of the rat. Correlation of intracellular pyruvate contents and pyruvate dehydrogenase activity. *Biochem. J.* **134**, 885–889 (1973).
45. V. Compan *et al*., Monitoring mitochondrial pyruvate carrier activity in real time using a BRET-based biosensor: Investigation of the warburg effect. *Mol. Cell* **59**, 491–501 (2015).
46. P. Kirk *et al*., CD147 is tightly associated with lactate transporters MCT1 and MCT4 and facilitates their cell surface expression. *EMBO J.* **19**, 3896–3904 (2000).
47. B. W. Kennedy, M. I. Kettunen, D. E. Hu, K. M. Brindle, Probing lactate dehydrogenase activity in tumors by measuring hydrogen/deuterium exchange in hyperpolarized l-[1-(13)C,U-(2)H]lactate. *J. Am. Chem. Soc.* **134**, 4969–4977 (2012).
48. H. N. Xu *et al*., Differentiating inflamed and normal lungs by the apparent reaction rate constants of lactate dehydrogenase probed by hyperpolarized (13)C labeled pyruvate. *Quant. Imaging Med. Surg.* **6**, 57–66 (2016).
49. P. E. Z. Larson *et al*., Investigation of analysis methods for hyperpolarized 13C-pyruvate metabolic MRI in prostate cancer patients. *NMR Biomed.* **31**, e3997 (2018).
50. A. P. Halestrap, M. C. Wilson, The monocarboxylate transporter family–role and regulation. *IUBMB Life* **64**, 109–119 (2012).
51. K. R. Keshari *et al*., Hyperpolarized 13C-pyruvate magnetic resonance reveals rapid lactate export in metastatic renal cell carcinomas. *Cancer Res.* **73**, 529–538 (2013).
52. Y. Takado *et al*., Hyperpolarized (13)C magnetic resonance spectroscopy reveals the rate-limiting role of the blood-brain barrier in the cerebral uptake and metabolism of l-lactate in vivo. *ACS Chem. Neurosci.* **9**, 2554–2562 (2018).
53. R. J. Simpson, K. M. Brindle, F. F. Brown, I. D. Campbell, D. L. Foxall, A p.m.r. isotope-exchange method for studying the kinetic properties of dehydrogenases in intact cells. *Biochem. J.* **202**, 573–579 (1982).
54. K. M. Brindle, I. D. Campbell, R. J. Simpson, A 1H-NMR study of the activity expressed by lactate dehydrogenase in the human erythrocyte. *Eur. J. Biochem.* **158**, 299–305 (1986).
55. C. Juel, A. P. Halestrap, Lactate transport in skeletal muscle - role and regulation of the monocarboxylate transporter. *J. Physiol.* **517**, 633–642 (1999).
56. A. P. Halestrap, The monocarboxylate transporter family—Structure and functional characterization. *IUBMB Life* **64**, 1–9 (2012).
57. E. M. Serrao *et al*., MRI with hyperpolarised [1-13C]pyruvate detects advanced pancreatic preneoplasia prior to invasive disease in a mouse model. *Gut* **65**, 465–475 (2016).
58. V. C. Sandulache *et al*., Evaluation of hyperpolarized [1-(1)(3)C]-pyruvate by magnetic resonance to detect ionizing radiation effects in real time. *PLoS One* **9**, e87031 (2014).
59. C. S. Hong *et al*., MCT1 modulates cancer cell pyruvate export and growth of tumors that co-express MCT1 and MCT4. *Cell Rep.* **14**, 1590–1601 (2016).
60. E. R. Plummer; Cancer Research UK, A phase I trial of AZD3965 in patients with advanced cancer. *ClinicalTrials.gov*, http://clinicaltrials.gov/show/NCT01791595 (2013).
61. N. J. Curtis *et al*., Pre-clinical pharmacology of AZD3965, a selective inhibitor of MCT1: DLBCL, NHL and Burkitt's lymphoma anti-tumor activity. *Oncotarget* **8**, 69219–69236 (2017).
62. A. Tasdogan *et al*., Metabolic heterogeneity confers differences in melanoma metastatic potential. *Nature* **577**, 115–120 (2020).
63. M. Eilertsen *et al*., Monocarboxylate transporters 1-4 in NSCLC: MCT1 is an independent prognostic marker for survival. *PLoS One* **9**, e105038 (2014).
64. A. Latif *et al*., Monocarboxylate Transporter 1 (MCT1) is an independent prognostic biomarker in endometrial cancer. *BMC Clin. Pathol.* **17**, 27 (2017).
65. X. Chen *et al*., Monocarboxylate transporter 1 is an independent prognostic factor in esophageal squamous cell carcinoma. *Oncol. Rep.* **41**, 2529–2539 (2019).
66. S. J. Park *et al*., An overview of MCT1 and MCT4 in GBM: Small molecule transporters with large implications. *Am. J. Cancer Res.* **8**, 1967–1976 (2018).
67. C. Pinheiro *et al*., Monocarboxylate transporters 1 and 4 are associated with CD147 in cervical carcinoma. *Dis. Markers* **26**, 97–103 (2009).
68. A. Sukeda *et al*., Expression of monocarboxylate transporter 1 is associated with better prognosis and reduced nodal metastasis in pancreatic ductal adenocarcinoma. *Pancreas* **48**, 1102–1110 (2019).
69. R. Le Floch *et al*., CD147 subunit of lactate/H+ symporters MCT1 and hypoxia-inducible MCT4 is critical for energetics and growth of glycolytic tumors. *Proc. Natl. Acad. Sci. U.S.A.* **108**, 16663–16668 (2011).
70. P. Dutta *et al*., Evaluation of LDH-A and glutaminase inhibition in vivo by hyperpolarized 13C-pyruvate magnetic resonance spectroscopy of tumors. *Cancer Res.* **73**, 4190–4195 (2013).